Additively Manufactured Iron-Based Bulk Metallic Glass Composite Electrocatalysts: Effect of Microstructural States on the Oxygen Evolution Reaction Activity

Jan Wegner, Ricardo Martínez-Hincapié, Viktor Čolić,* and Stefan Kleszczynski*

The influence of crystallinity on the electrocatalytic activity of complex alloys requires further clarification to optimize their properties. In this work, the electrocatalytic properties of additively manufactured Fe-based bulk metallic glasses (BMG), namely, their activity toward the oxygen evolution reaction are studied in alkaline media. Laser powder bed fusion (PBF-LB/M) is applied to fabricate electrodes with different numbers of glass-forming $Fe_{75}Mo_{14.3}Ni_{1.6}P_6C_{2.2}B_1$ layers on 316L stainless steel substrates. Electrochemical and physicochemical characterization techniques are used to characterize the surface of the electrodes both as-built and after annealing and devitrification. Although different process parameters lead to similar electrochemical responses, certain differences are observable. Namely, the thickness of the BMG-coating and the ratio of crystalline/amorphous phases seems to determine the catalytic activity. In particular, it is noticeable that partially crystallized samples display higher activities, contrary to some previous observations on different materials. The measurements indicate a complex interplay between crystallinity and active surface area that determines the electrochemical properties of the investigated electrode material.

1. Introduction

The oxygen evolution reaction (OER; $4OH^- \rightarrow 2H_2O + O_2 + 4e^-$, in alkaline or $2H_2O \rightarrow O_2 + 4e^- + 4H^+$, in acidic media) is key for the development of more efficient energy storage and conversion systems (e.g., alkaline/PEM electrolyzers and batteries).[1–6] The OER is a complex reaction that involves four electron–proton transfers involving multiple reaction intermediates. In particular, for the OER the $(\Delta G^0_{O*} - \Delta G^0_{HO*})$ descriptor has been used to explain the electrocatalytic behavior observed on numerous materials.[7] Nonetheless, optimizing the binding energy for each intermediate is challenging due to the limitations imposed by the scaling relations.[8–10] Iridium- and ruthenium-based materials are considered the most active catalysts as OER electrodes in acidic media.[11] However, these elements are scarce and costly, hampering large-scale applications. Furthermore, even though Ir- and Ru-based electrocatalysts are comparatively stable, both materials can dissolve under the high anodic potentials present during the OER.[12] In alkaline media, nickel-, cobalt-, manganese-, and iron-based catalysts are preferably used, due to their high abundance and suitable electrocatalytic activity.[5,6,13,14] Investigations on organometallic, chalcogenides, and metal pnictide catalyst systems report promising results, potentially representing an alternative to metal oxide materials.[15–18] Nevertheless, electrocatalysts for OER need high overpotentials to reach industrially relevant currents (100–1000 mA cm^{-2}).[3,19] Therefore, the development of new, highly active, and abundant materials is required to proliferate technologies like alkaline electrolyzers, where the OER is the bottleneck for their further development.[3] The OER is a structure-sensitive reaction, e.g., RuO_2 (001) has a higher activity than RuO_2 (110) or RuO_2 (111) orientations in acidic media.[20] Also, it has been observed that amorphous arrangements of NiFe-catalysts have higher catalytic activity compared to their crystalline counterparts.[21] A deeper understanding of the relations between surface structure and reactivity could allow for more sophisticated alloy- and microstructural designs.[22] However, in oxide materials commonly used for water oxidation, this is not a trivial problem; even more so when nanoparticles are used instead of bulk materials since they are prone to reconstruction or dissolution surface-processes.

In recent years, metallic glasses (MGs) emerged as promising materials to create electrocatalytic surfaces with unique active sites. Additionally, advanced processing technologies allow the selective tailoring of the microstructure to a certain degree.[7,23] The desirable physicochemical properties of MGs originate

J. Wegner, S. Kleszczynski
Chair of Manufacturing Technology
University of Duisburg-Essen
47057 Duisburg, Germany
E-mail: stefan.kleszczynski@uni-due.de
R. Martínez-Hincapié, V. Čolić
Electrochemistry for Energy Conversion
Max-Planck-Institute for Chemical Energy Conversion
D-45470 Mülheim an der Ruhr, Germany
E-mail: viktor.colic@cec.mpg.de
V. Čolić, S. Kleszczynski
Center for Nanointegration Duisburg- Essen (CENIDE)
47057 Duisburg, Germany

from the amorphous atomic arrangement of their constitutional elements. The absence of crystalline defects leads to near theoretical strength and is associated with enhanced corrosion resistance.[24] Their application in electrochemistry could shed light on the effects of crystallinity, strain, and surface structure on electrochemical properties. For the OER in particular, nanoporous metallic glasses containing mainly nickel and iron display outstanding performance in acid and alkaline conditions. Hu et al. fabricated amorphous $Ni_{40}Fe_{40}P_{20}$ electrodes via melt spinning and quenching of ingots.[25] Electrochemical measurements revealed a high activity for the OER, reaching a 10 mA cm^{-2} current value with an overpotential of only 219 mV.[25] The outstanding performance was rationalized in terms of the synergistic effects of the alloy constituents: nickel, iron, and phosphate, along with the increase in the surface area. Jin et al. designed and prepared through arc-melting a group of nanoporous Fe-Ni-Co metallic glasses that reach the value of 10 mA cm^{-2} with an overpotential of only 274 mV in 1 M KOH.[26]

However, manufacturing of MGs, especially as extended surfaces, remains challenging. The vitrification of the melt requires rapid quenching, which inherently limits the size and complexity of the processed parts. Comprehensive alloy development in recent decades established so-called BMGs, that can be cast into rods with diameters > 1 mm. Yet, their vitrification requires cooling rates of ≈1–100 K s^{-1}, which remains a drawback in manufacturing large and sophisticated geometries. Additive manufacturing (AM) through laser powder bed fusion of metals (PBF-LB/M) recently developed as a promising methodology to overcome these restrictions.[27,28] During PBF-LB/M, powder layers of 20–100 µm are subsequently deposited and locally fused by a focused laser beam, which is deflected by a scanner system. The small melt pools and rapid laser-material interactions lead to transient cooling rates of 10^6 K s^{-1}.[29] The stepwise approach decouples the local thermal history from the overall part geometry. Consequently, many glass-forming alloys can theoretically be processed via PBF-LB/M, widely independent of the part size or geometry. Albeit high residual stresses and oxygen adsorption of the powder remain challenging during PBF-LB/M fabrication of BMGs, as both are associated with cracking and partial crystallization in additively manufactured BMGs.[30,31] Fe-based BMGs are particularly associated with a low fracture toughness which can lead to severe crack formation.[27,32–35] In this matter, the applied processing parameters are crucial for an amorphous, crack-formation, and dense processing. Generally, the energy input during the laser exposure needs to ensure the complete fusion of the powder particles into a dense part. Optimization of the energy input is not trivial and requires extensive parameter studies. If the energy input is too high, cooling rates decrease and may lead to undesired crystallization in BMGs. Thus, the applied energy input needs to be carefully chosen to successfully fabricate amorphous parts.[30,36,37] A widely used approach to quantify the energy input is the line energy density (E_L), which defines the ratio between the applied laser power (P), and the scanning speed (v).[38] Since this approach neglects factors such as absorptivity, melt pool dynamics, and laser profile, its validity is limited to qualitative comparisons rather than a physical description of the energy balance.[39]

Only a few studies on the applicability of PBF-L/M-processed MGs or BMGs for electrochemical applications are reported so far.[40,41] Liang et al. recently investigated the catalytic performance of PBF-LB/M fabricated rhombic dodecahedron structured $Fe_{70}Cr_5Ni_3Mo_3W_9Si_5B_5$.[40] The partially crystalline samples revealed a superior catalytic ability for a Fenton-like process to degrade a BR3B-A dye in terms of reaction rate and activation energy in comparison to conventionally manufactured MGs and crystalline alloys.

In this study, we evaluate a PBF-LB/M processed Fe-based BMG with surface science techniques and its electrochemical characterization. A hybrid manufacturing approach is chosen, where a thin BMG coating is applied to a steel substrate via PBF-LB/M (see Section 4). The method allows to minimize the necessary amount of powder for the investigated alloy and reduces interfering factors such as cracking. Additionally, it allows a quick evaluation of the fundamental usability of Fe-based BMGs without the need for a complex parameter study. The selected approach is transferable to other material systems and potentially enables the characterization of large numbers of alloy composition. This provides an opportunity to explore the structural sensitivity of OER in BMG/electrolyte interphases and to screen for new materials for this application.
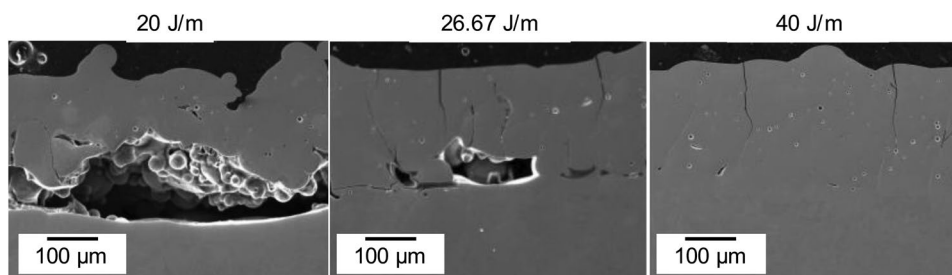
2. Results and Discussion

2.1. Physicochemical Characterization

Figure 1 displays scanning electron microscope (SEM) images of three microsections from typical electrodes after adding 15 Fe-BMG layers (with a respective nominal layer thickness of 20 µm) processed with different PBF-LB/M parameters. Complementary low-magnified light optical microscopy (LOM) images of a cross-section are provided in Figure S1 (Supporting Information).

Each sample was processed with different energy densities ranging from 20 to 40 J m^{-1}. Within the $Fe_{75}Mo_{14.3}Ni_{1.6}P_6C_{2.2}B_1$ layers, spherical pores indicate gas entrapment. This can be an indication that the energy input is not yet optimally adjusted. Despite the small volume of the applied BMG layers, vertical cracks can be observed. These can be traced back to the low fracture toughness of Fe-based BMGs combined with the high residual stresses that appear during PBFLB/M.[27,33,42] One should bear in mind, that the mechanical properties associated with these structural defects deteriorate the suitability for most technical applications. Recent findings indicate, that further process optimization, such as the application of adjusted scan strategies[43] and alloy adjustment[44,45] can be applied to fabricate crack-free Fe-based BMGs through PBF-LB/M. However, since the evaluation in this work merely targets the general electrochemical and physicochemical characterization in short-term conditions, further optimization of the residual stresses was dispensed. This will be the subject of further investigations.

The quality of the interface between the 316L substrate and the $Fe_{75}Mo_{14.3}Ni_{1.6}P_6C_{2.2}B_1$ coating appears dependent on the applied energy density. For the lowest energy density (20 J m^{-1}), large pores and delamination are visible. The number and size of such defects in the interface gradually decrease with increasing the applied energy density. At the highest density of 40 J m^{-1}

2202499 (2 of 11)

**ADVANCED
SCIENCE NEWS**

www.advancedsciencenews.com

**ADVANCED
MATERIALS
INTERFACES**

www.advmatinterfaces.de

Figure 1. SEM images of a electrodes with 15 layers of $Fe_{75}Mo_{14.3}Ni_{1.6}P_6C_{2.2}B_1$ applied with 20, 26.67, and 40 J m^{-1}.

sufficient bonding between both alloys is observed. Generally, higher energy input during the melting leads to larger melt pools. This fosters the fusion between the 316L substrate and the applied BMG-layers. One can assume, that an intermixing of the glass-forming $Fe_{75}Mo_{14.3}Ni_{1.6}P_6C_{2.2}B_1$ with the Cr-rich 316L substrate may alter its glass-forming ability and electrochemical activity. Energy-dispersive X-ray spectroscopy (EDX) measurements were conducted to evaluate the intermixing of the alloys.

Figure 2 displays an SEM-image (BSD Detector) and EDX mappings of an electrode with 15 $Fe_{75}Mo_{14.3}Ni_{1.6}P_6C_{2.2}B_1$ layers added (processed with 40 J m^{-1}). A clear interface between the 316L-substrate and the $Fe_{75}Mo_{14.3}Ni_{1.6}P_6C_{2.2}B_1$ layers is visible through the deviant gray values in the BSD-image. At higher magnification, whirl-like structures indicate partial crystallization and intermixing with the base material (highlighted by the inset) in the transition zone.

The EDX-mappings reveal a widely uniform distribution of Fe (B) and Mo (C) as main components for the glass-forming alloys. Ni (D) and Cr (E) mappings mark the 316L substrate, since Cr is exclusively present in 316L and Ni is present in a distinctively larger fraction. Interestingly, Ni- and Cr-enriched areas can be found in the BMG-coating which are accompanied by the impoverishment of Fe. Here intermixing with the 316L together with precipitation of Cr- and Ni-rich phases can be assumed. However, an in-depth investigation of this

observation was not in the scope of this investigation but is subject to ongoing research.

Figure 3 displays the Mo and Cr-Content within a sample with 15 (A) and 5 (B) added layers of $Fe_{75}Mo_{14.3}Ni_{1.6}P_6C_{2.2}B_1$ measured vertically along the building height (compare Figure S2, Supporting Information). For the sample with 15 layers (≈300 μm), a stable Mo-Content of 14 mass% indicates a widely homogenous BMG layer within the first 175 μm. Subsequently, the Moconcentration decays with simultaneously increasing Cr-amount which represents the intermixing of the substrate with the electrode material within a transition zone of 75 μm. The transition zone originates from the fusion of the two alloys, which depends on the melt pool depth of each layer and the resulting overlap between two layers. The depth of melt pools during PBF-LB/M depends on various factors such as the packing density of the powder bed, the layer thickness, and the alloy composition. Typical melt pool depths in commercial applications range from 42 to 94 μm.[46] In a distance of 250 μm from the surface, only the 316L substrate is observed. Consequently, the actual layer thickness of the Fe-based BMG is drastically reduced compared to the nominal thickness of 300 μm which is associated with 15 layers. This can partially be attributed to the shrinkage during the powder melting, the remaining surface roughness of the substrate surface, and the transition zone between the two alloys. Samples with five
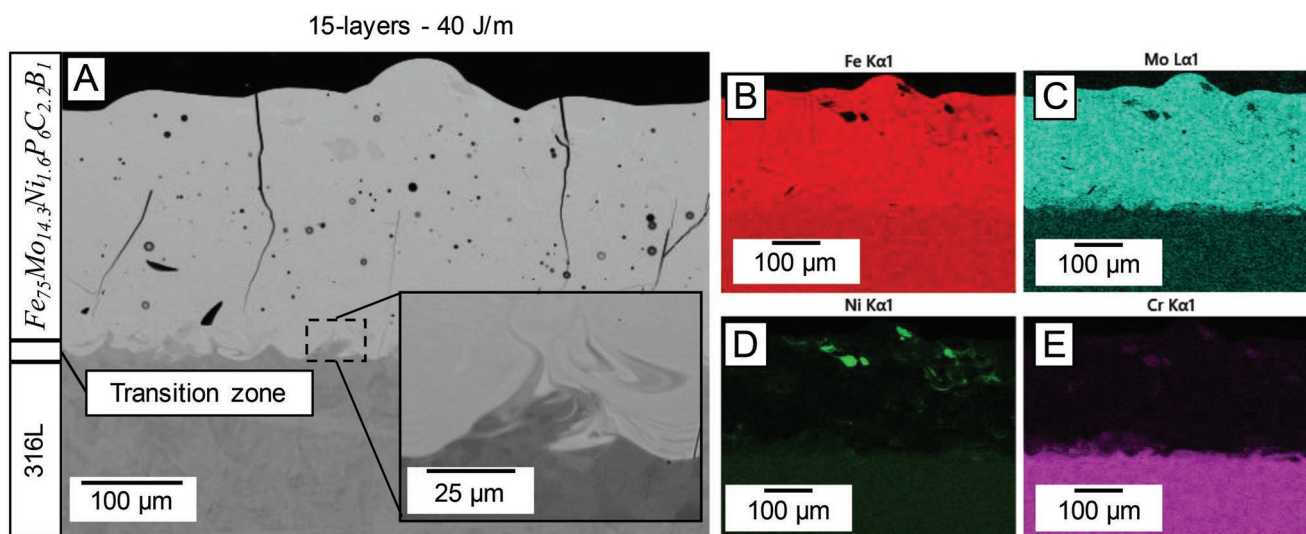
Figure 2. SEM-BSD image A) of an electrode with 15 layers of $Fe_{75}Mo_{14.3}Ni_{1.6}P_6C_{2.2}B_1$ applied with processed with 40 J m^{-1}. EDX-Mapping of the elements Fe B), Mo C), Ni D), Cr E).
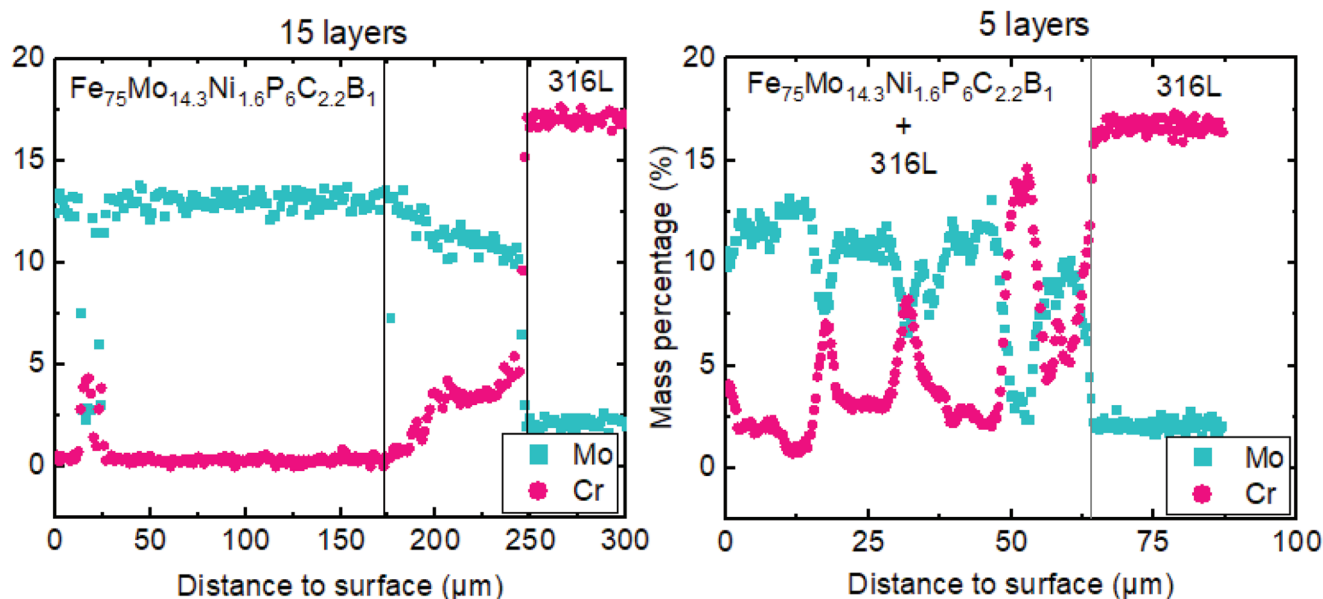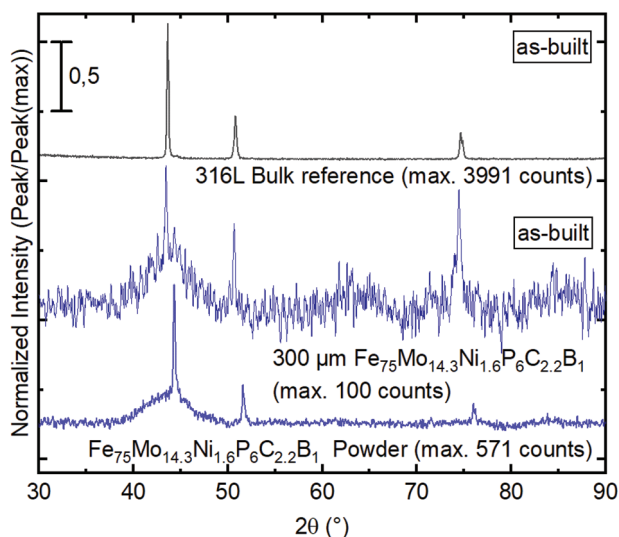
Figure 3. Vertical EDX-Line Scans along the build height for Mo and Cr for an electrode with 15 layers A) and 5 layers B) of $Fe_{75}Mo_{14.3}Ni_{1.6}P_6C_{2.2}B_1$ processed with 40 J m^{-1}. Gray vertical lines indicate the transition zone between the investigated materials. Note that the diagrams use a different scale resolution on the x-axis.

BMG layers added show no stable Mo-content but instead fluctuations of Mo and Cr implying a coexistence of material from the 316L substrate and $Fe_{75}Mo_{14.3}Ni_{1.6}P_6C_{2.2}B_1$ on the surface of such electrodes.

Samples with 15 added layers processed with an energy density of 40 J m^{-1} display a low defect density and a mostly homogenous $Fe_{75}Mo_{14.3}Ni_{1.6}P_6C_{2.2}B_1$ surface. X-ray diffraction (XRD) measurements taken of the sample surfaces are displayed in **Figure 4**. The 316L bulk reference reveals the typical XRD pattern of the fcc cell of Fe (γ-Fe), as expected for austenitic steel.[42–44] The $Fe_{75}Mo_{14.3}Ni_{1.6}P_6C_{2.2}B_1$ powder shows
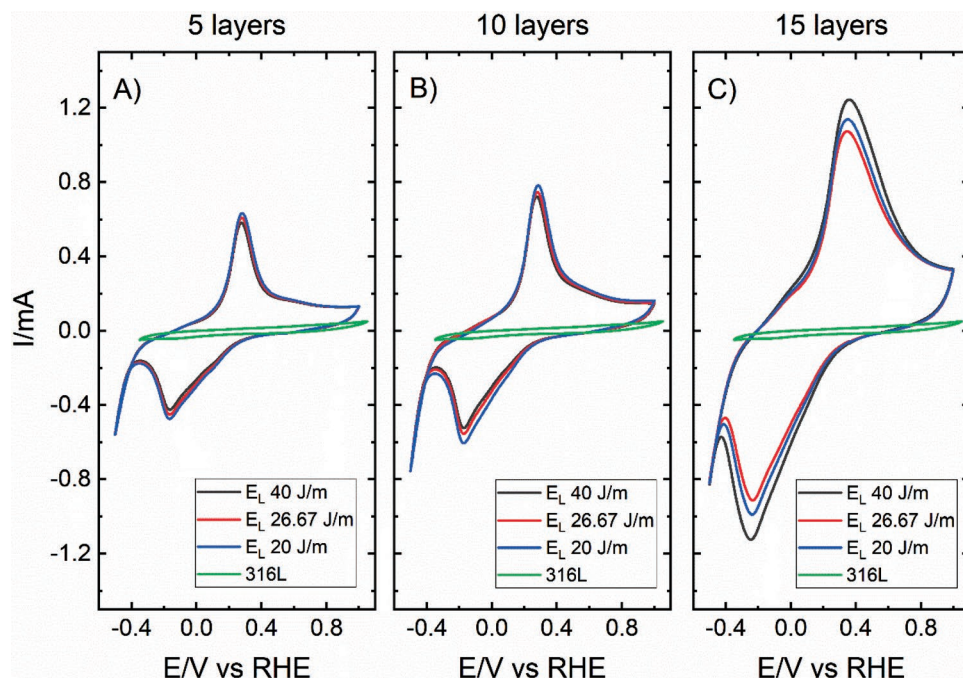
a broad and diffuse diffraction maximum at ≈43° 2θ which is a characteristic for amorphous materials. Discrete peaks superimposing the amorphous halo at 44°, 51°, and 72° 2θ indicate fractions of γ-Fe crystals in the powder feedstock. This can be attributed to larger particles in the feedstock, which experience lowered cooling rates during the PBF-LB/M-melting. Eventually this leads to crystallization, especially for compositions with limited glass-forming ability.[45] The sample with 15 added layers of $Fe_{75}Mo_{14.3}Ni_{1.6}P_6C_{2.2}B_1$ shows a distinct drop in the signal counts and resembles the halo of the mainly amorphous powder. However small diffraction peaks of γ-Fe crystals are superposed by the halo indicate the presence of crystalline fractions within the amorphous layers. In view of the EDX results discussed earlier, this might be attributed to the partial intermixing of the $Fe_{75}Mo_{14.3}Ni_{1.6}P_6C_{2.2}B_1$ with the 316L substrate. However, due to the penetration depth of the X-ray beam, a measurement artifact cannot be excluded.

2.2. Electrochemical Characterization

Figure 5 shows typical voltammograms of the as-built electrodes in Ar-saturated 0.1 M NaOH, featuring five (≈100 μm), ten (≈200 μm), or 15 (≈300 μm) layers of $Fe_{75}Mo_{14.3}Ni_{1.6}P_6C_{2.2}B_1$ fabricated with different E_L. The electric connection was made using copper wire and copper tape trying to assure the best electrical contact possible. The experiments were carried out using the hanging meniscus configuration to assure that only the Fe-BMG is in contact with the working solution and not the substrate. It is clear that the overall response is similar in all electrodes regardless of the process parameters used to fabricate the electrode (e.g., E_L). However, in some electrodes fabricated with 20 J m^{-1}, the impedance measured at the open circuit potential is too high to carry out the electrochemical

Figure 4. XRD-results of a PBF-LB/M processed 316L surface, glassy $Fe_{75}Mo_{14.3}Ni_{1.6}P_6C_{2.2}B_1$ powder, and as-built samples 15 layers (≈300 μm) of $Fe_{75}Mo_{14.3}Ni_{1.6}P_6C_{2.2}B_1$ added with 40 J m^{-1}.

Figure 5. Cyclic voltammograms of as-built Fe-based BMG electrodes in Ar-saturated 0.1 M NaOH with different thicknesses of Fe BMG layers A) 5 layers, B) 10 layers, and C) 15 layers. Scan rate: 50 mV s^{-1}. The electrochemical response of the 316L electrode is shown for the sake of comparison.

experiment, indicating high resistivity. For all electrodes, a peak around 0.30 V appears in the positive-sweep direction, whereas in the negative-sweep the peak is located around –0.20 V, in close agreement with previous results reported for pure iron electrodes.[46,47] Small differences could be a consequence of the other elements present, mainly Mo. It is striking, that the current response scales with the number of layers applied on the 316L substrate. The electrode with five layers exhibits a current range of ≈0.6 mA which gradually increases to 0.8 and 1.2 mA for 10 and 15 layers, respectively. In view of the EDX analysis in Figure 3, this could be the result of the increased overlap between the Fe$_{75}$Mo$_{14.3}$Ni$_{1.6}$P$_6$C$_{2.2}$B$_1$ – 316L transition zone and the surface. For comparison, the voltammetric response of the uncoated steel substrate (316L) is also shown, underlining the prominent effect of the Fe-BMG layers on the electrochemical behavior.

The catalytic activity of the Fe BMG electrodes for the OER was evaluated using linear scanning voltammetry (LSV). For all OER experiments, the uncompensated resistance (R_u) was determined from electrochemical impedance spectroscopy (EIS) and used with automatic compensation of 85%.[48] The rest of the R_u was taken into account during data processing. Here it is important to note that the meniscus configuration could give higher resistance in comparison with a non-meniscus three electrode setup due to the increased distance between the RE's capillary and the working electrode. However, the obtained uncompensated resistance, R_u, value was consistently between 50 and 100 Ohms throughout all experiments. In addition, we use the geometrical surface area to normalize the results. To evaluate the impact of the microstructure on the catalytic performance, the largely amorphous samples were objected to a heat treatment to increase the crystalline fractions in com-

parison to the as-built state. The annealing temperature was set to 873 K which is roughly 50 K above T_x in accordance with the DSC results of the amorphous powder material (Figure S3, Supporting Information). The effect of the oven treatment on the structure was assessed by XRD measurements (see **Figure 6**). After annealing the Fe$_{75}$Mo$_{14.3}$Ni$_{1.6}$P$_6$C$_{2.2}$B$_1$ samples at 600 °C for 15 min, distinct crystalline peaks replace the previously amorphous halo. However, the broad character of the peaks still indicates small and distorted crystallites. It is clear, that the heat treatment increases the crystalline fraction in the electrodes.

Figure 7 illustrates the LSV obtained for fresh "as-built" electrodes before and after the crystallization heat treatment. The 5-layer (≈100 μm) Fe-BMG electrode showed the highest OER activity, followed by the 300 and 200 μm electrodes as evidenced by the overpotential to reach the same current density (5 or 10 mA cm^{-2}, **Table 1**).

In addition, the apparent onset potential is the lowest in the 100 μm electrode, although the other electrodes show similar onset potentials as well. It is clear, that any electrode fabricated with more than 100 μm of the Fe-BMG had a significantly higher activity compared to the 316L substrate. In contrast to the behavior of the voltammograms in Figure 5, an increase in the thickness of BMG layers does not linearly increase the activity for the OER. In fact, the electrodes with five layers appear more active than electrodes that have 10 or 15 layers (100, 200, and 300 μm, respectively). Thus, despite the intermixing with the 316L substrate as indicated by the EDX results in Figure 3, the partial intermixing of the Fe$_{75}$Mo$_{14.3}$Ni$_{1.6}$P$_6$C$_{2.2}$B$_1$ coating does not deteriorate the activity. Here, it is worth mentioning that the processing conditions such as E_L appear to be insignificant for the resulting OER activity. However similar to the observations during the electrochemical characterization (Figure 5),
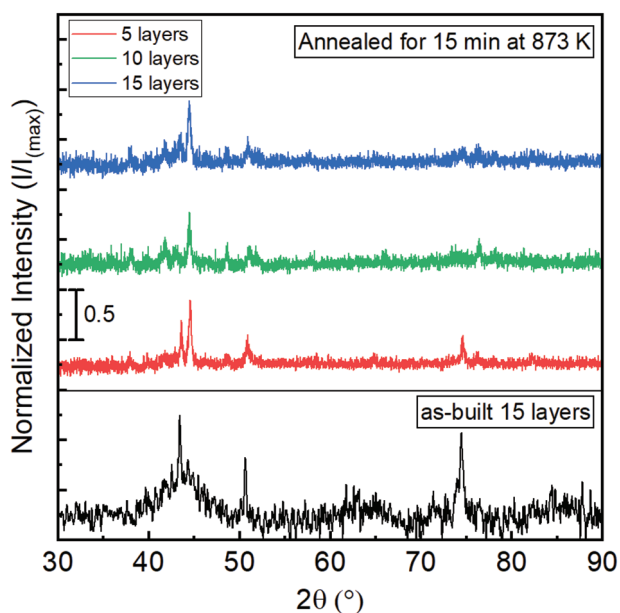
Figure 6. XRD results of selected samples of the annealed samples for the investigated number of layers processed with 40 J m^{-1}. The diffractogram of an as-built electrode with 15 layers is additionally provided as a nearly amorphous reference.

electrodes fabricated with 20 J m^{-1} and, to a lesser extent with 26 J m^{-1}, featured limited reproducibility in their OER response among different samples. Several studies have suggested that the E_L has an influence on the structural properties of PBF-LB/M manufactured materials such as texture, porosity, and microstructure.[30,49,50] However, likely to the relatively narrow E_L-range investigated here, the structural features are similar
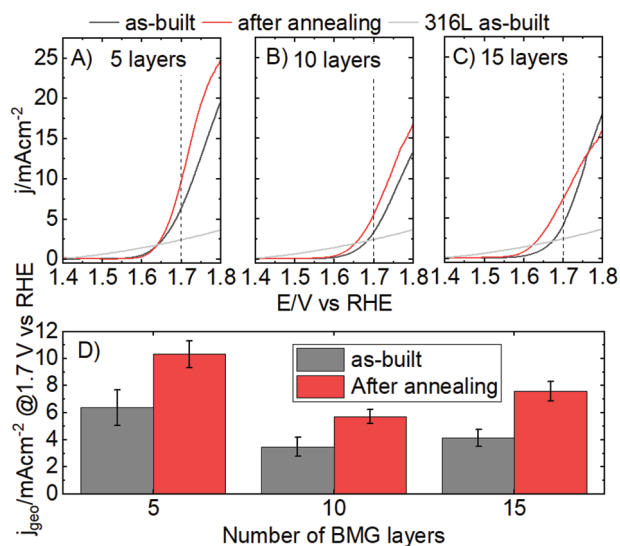
Figure 7. OER polarization curves of as prepared (black) electrodes and ones after furnace treatment (red), with different thicknesses of $Fe_{75}Mo_{14.3}Ni_{1.6}P_6C_{2.2}B_1$-layers A) 5 layers ($\approx$100 µm), B) 10 layers ($\approx$200 µm), and C) 15 layers electrodes ($\approx$300 µm). Scan rate 5 mV s^{-1}. The response of the 316L substrate (gray) is included for the sake of comparison. D) Current density at 1.7 V for different electrodes before (black) and after (red) heat treatment.

regardless to the applied E_L. To further assess the impact of different microstructural states, samples were annealed, as described earlier. The testing of the OER activity after the heat treatment reveals that the general trends are similar to those found in the as-built electrodes, however, some subtle changes are observed. In particular, the 15-layer electrode has the lowest onset potential after the treatment (see Figure 7).

The OER current at a constant potential of 1.7 V versus RHE before and after the heat treatment is juxtaposed in Figure 7D. It can be observed that the activity increases after the annealing process for all electrodes. This behavior appears regardless of the potential chosen for comparison, showing that the heat treatment improves the OER activity. It has been stated that the conductivity and impurities could explain the experimental trends observed for the OER.[51] Here, we used the NaOH reagent with the highest commercially available purity, however, the possible presence of small Fe-impurities should not be excluded. Nonetheless, since the electrodes already have a high iron content the influence of adventitious Fe-impurities in the working solution is likely negligible. It was shown previously that crystalline structures tend to have a higher conductivity than their amorphous counterparts (if the composition is the same) as a result of the short-range order in amorphous solids that limits the mean free path for electrons.[52,53] In order to evaluate the possibility that the increase in the electrocatalytic activity is related to changes in the chemical surface composition, X-ray photoelectron spectroscopy (XPS) was used to investigate the electrodes before and after the heat treatment, and the OER (**Figure 8**).

The C1s peak (284.8 eV) was used to calibrate the binding energies in the spectrum. In the Fe 2p peak, the Fe 2p3/2 appears at 711.0 eV in all measurements. Moreover, the Fe 2p1/2 peak in the as-built electrode (724.1 eV) showed lower binding energy than electrodes after HT and after the electrochemical reaction (725.2 eV) (Figure 8A). The results suggest that the Fe components are stable under the reaction conditions. For the Mo 3p spectrum the contrary is observed (Figure 8B). In the as-built electrode, no Mo 3p1/2 peak is sampled. However, after the HT and after the EC experiment, characteristic Mo 3p1/2 signal at 416.6 and 398.4 eV (Mo 3p3/2) are detected. To complement the analysis of the Mo 3p, the Mo 3d spectra were also analyzed. As shown in Figure S4 (Supporting Information), the results are similar to those obtained in the analysis of Figure 8B. The Mo 3p1/2 signal in the as-built electrode is lower, compared to the electrodes after the HT treatment and after the EC experiment. These data suggest that Mo segregates to the surface of the Fe-BMG electrode after the HT and during the OER. Complementary to that, Figure S5 (Supporting Information) shows the XPS spectra for P, Ni, and B. Although the concentration of these elements is low in the precursor, it is well-known that the surface composition can change during and after the OER.[54–56] In the as-prepared electrodes, no signal corresponding to P, Ni, or B is detected. However, after the HT and the electrochemical experiments the signal corresponding to these elements is clearly visible. In particular, the presence of nickel after the HT could be responsible for the increase of the electrocatalytic activity, since it has been demonstrated that Ni-Fe oxyhydroxide is a highly active species for the OER.[57]

Table 1. Tafel slope at low and high overpotential for as prepared electrodes and after heat treatment (*), also the overpotential for a geometrical current of 5 and 10 mA cm^{-2}.

| Electrode	Low η [mV dec^{-1}]	Overpotential @5 mA cm^{-2} [V]	Overpotential @10 mA cm^{-2} [V]
0.1 mm	94	0.45	0.50
0.1 mm*	70	0.44	0.47
0.2 mm	87	0.49	0.54
0.2 mm*	85	0.46	0.51
0.3 mm	90	0.47	0.52
0.3 mm*	98	0.44	0.50

Since the surface chemical composition is not altered in a high extent by the heat treatment and the Fe oxidation state is the same before and after HT, we consider that the increase in the crystalline fraction in the glassy surface effectively leads to changes in the electrochemical properties. Considering that the electrode with 10 layers is less active than the one with five layers, although it is intermixed with the less active 316L substrate, one must consider the role of the active surface area. As the number of layers increases, the probability of structural defects (porosities and cracks) becomes higher (Figures S1 and S2, Supporting Information) which could affect the electrochemical response. In this work, the geometric area of the BMG electrodes has been used to normalize the results. However, to distinguish between the intrinsic electrocatalytic activity of the material and area-dependent activity, the current must be normalized with the respective electrochemical active surface area (ECSA). While there are established methods to estimate the ECSA of platinum or of metal-oxide electrodes, the determination of the ECSA of a multicomponent surface oxides requires standardization and significant work in both standard sample preparation and characterization.[58] Normalization of the current was done under the assumption, that the charge involved

in the redox transition observed in Figure 5 is proportional to the ECSA. However, constants similar to those available for platinum (210 µC cm^{-2}) or nickel (540 µC cm^{-2}) electrodes, which allow the conversion of charge to ECSA are not available for the alloy studied. Figure S6 (Supporting Information) shows the LSV of the electrodes using an estimated constant of 300 µC cm^{-2} to normalize the values of charge obtained. The value was estimated under the assumption that only the metal atoms of the constituents of the Fe-based BMG on the immediate surface undergo a single electron process on an ideally tessellated smooth surface. This highly idealized case is likely an underestimation. However, due to the lack of more empirically exact values, it serves here for demonstrative purposes. In this case, the most active electrode is the one with 5 layers, followed by the ones with 10 and 15 layers, respectively. Comparing the current at a potential value of 1.7 V versus RHE the trend is different from the one observed in Figure 7 since when the estimated ECSA is used to normalize the results the electrode with 10 layers is more active than the one with 15 layers (Figure S6, Supporting Information). In all the electrodes, the current is higher after the heat treatment.

In order to gain more information about the role of the ECSA, CVs at different scan rates (5, 10, 20, 30, 40, 50, 80, 100, 150, and 200 mV s^{-1}) were performed in the potential range 0.8–1.0 V versus RHE (Figure S7, Supporting Information) to obtain the double layer capacitance (C_{dl}). The average of the anodic and cathodic current was then plotted against the scan rate. An allometric fit was used for the linear regression, as this type of regression works better in cases where the system is not ideal.[59] Figure S8 (Supporting Information) shows the results of the allometric fitting. The ECSA of electrodes before and after the heat treatment was calculated in order to evaluate the current density (although this method can introduce large errors, up to a factor of 7[60]). The double layer capacitance values for all electrodes were divided by the specific capacitance (0.04 mF cm^2). The resulting ECSA values were used to
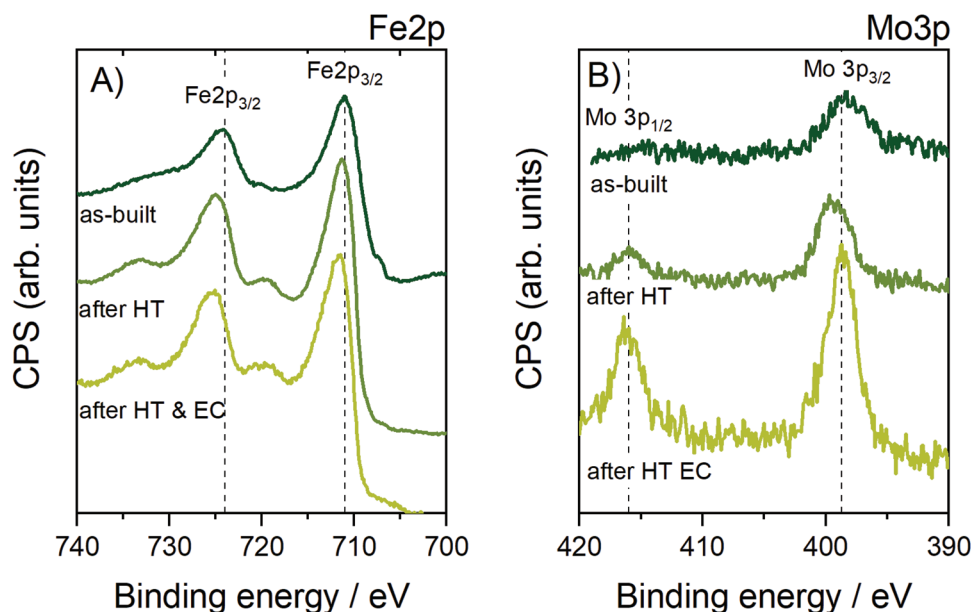
Figure 8. Fe 2p A) and Mo 3p B) high-resolution XPS spectra of 15 layers Fe-BMG electrodes before and after the heat treatment & OER.
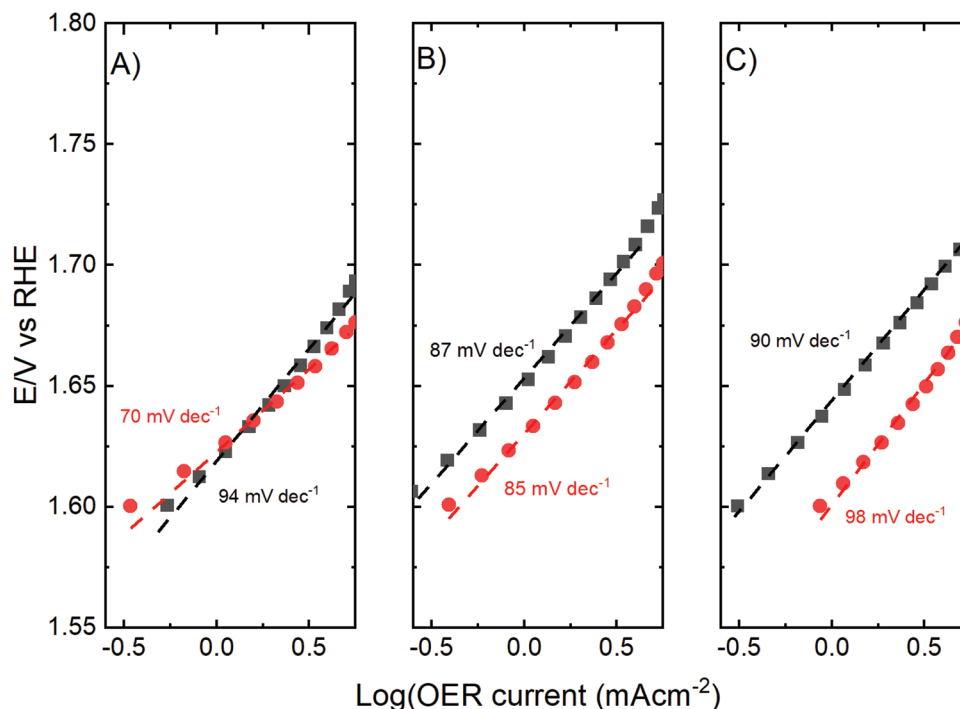
Figure 9. Tafel slopes for as-prepared (black) and postfurnace treatment electrodes (red) in low overpotential regions of different thicknesses of Fe BMG layers A) 5 layers, B) 10 layers, and C) 15 layers electrodes.

normalize the OER activity (Figure S9, Supporting Information). Using the ECSA instead of the geometric area clearly changes the results obtained for the 5 layer electrodes (see Figure S9, Supporting Information). However, it should be noted that significant intermixing was observed for this electrode. For electrodes with 10 and 15 layers, no changes are observed, and the electrodes are more active after the heat treatment.

There is likely an interplay of several factors that can increase or decrease the activity with the increasing number of deposited $Fe_{75}Mo_{14.3}Ni_{1.6}P_6C_{2.2}B_1$ layers. A thicker BMG layer reduces intermixing with the 316L substrate. However, more BMG material might decrease the conductivity due to its amorphous nature, which is also detrimental for OER-reaction, although we have not observed significant increases in impedance during EIS measurements. Finally, the heat treatment of the samples partially devitrifies the glassy surface, which enhances the conductivity and the electrochemical performance. The interplay between these effects likely produces an optimum at a certain thickness value, in this case being around five layers.

To date, the structural sensitivity of the OER is somewhat debated for various materials. The results coming from well-defined structures should be taken with care since at the OER potentials typical structures undergo surface reconstruction.[61] However, studies using RuO_2, Au, or IrOX reveal structural sensitivity trends,[62–65] for rutile ruthenium oxide the (100) and (101) orientations are more active than (110) or (111) orientations,[65] whereas for gold the most active orientation is the most open surface (110). [63] Investigations of amorphous materials are also significant since the defective structure offers unique sites and potentially higher surface area than crystalline counterparts.[66–68] The amorphous versus crystalline state of materials in relation to the OER catalytic activity is an important topic nowadays given the importance of this reaction for energy conversion devices. Some results imply that the short-range order in amorphous materials triggers the formation of specific active sites as a result of the electrochemical activation.[21] On the other hand, the crystalline materials can be more stable in the harsh conditions of the OER.[69]

Tafel slopes were calculated at low overpotentials to gain information about the apparent mechanism in the different electrodes. **Figure 9** displays the data and the Tafel-slopes, and the values are given in Table 1. At low overpotentials, all electrodes exhibited slopes between 60 and 100 mV decade^{-1}. The values reported here must be analyzed with great care for several reasons. First, mass-transfer effects should not be excluded, which could be especially important in the most porous electrodes, in addition, the presence of oxygen bubbles could complicate the analysis. Finally, non-noble materials are prone to undergo transformations during the course of the reaction, therefore, the thermodynamic conditions necessary to perform the analysis are not completely satisfied during the OER. Nevertheless, it is important to note that the Tafel slopes for all the electrodes increase after the heat treatment, except for the one with five layers where the Tafel slope decreases (from 94 to 70 mV dec^{-1}) at low overpotentials. It is noticeable, that the overpotential at almost any current indicates a higher activity of the electrodes after the heat treatment (compare Figure 7). In an apparent contradiction, the Tafel slopes are higher after the heat treatment. Tafel slope and overpotential are two values that could be relatable, however, the values do not depend on each other. [70]

The long-term stability of electrodes is crucial for their practical application.[71,72] The tough conditions, i.e., pH, potential, and temperature at which the OER takes place, in addition to the bubble formation can result in severe electrocatalysts (de)activation. An active and selective electrode that degrades in short periods is not an acceptable option (unless it is used to manufacture high price products). To evaluate the stability of the Fe BMG electrodes under catalytic conditions, electrodes with different numbers of Fe BMG layers before and after the heat treatment were evaluated using chronopotentiometry with an applied constant current density of 5 mA cm^{-2}. Figure S11 (Supporting Information) shows the electrochemical stability of the electrodes. In general, all the electrodes are stable under the conditions (current and time) applied here. However, it is important to mention that the current value used to evaluate the stability of the electrodes is not from an industrial point of view relevant. Additionally, jump-like discontinuities in the $I = f(t)$ curve suggest that the formation and detachment of bubbles still has a pronounce effect on the experimental results. Furthermore, the use of common current values used in the access of the electrochemical stability, i.e., 10 or 100 mA cm^{-2} or time (at least 24 h) with these electrodes has failed. The incapacity to remove the bubbles generated during the OER could be the most plausible explanation for this behavior.

Here, we use stain steel (SS) as subtract to fabricate the Fe BMG not only because it is an excellent cost-effective current collector in water electrolysis but also because is an excellent option for the AM process. Another point that deserves our attention regarding the SS is their intrinsic activity for the OER.[73,74] Recently Schäfer and Chatenet groups SS could be a very active material for the OER.[74–77] This factor should be considered when the electrocatalytic activity of Fe BMG electrodes supported in SS is evaluated. Following a similar procedure to the one used in ref. [74] allows for accelerating the aging of the electrodes and at the same time prevents bubble formation. The concentration of iron, nickel, and chromium in the working solution was assessed using via inductively coupled plasma-optical emission spectrometry (ICP-OES 5100 SVDV, Agilent) to evaluate the concentration of the possible dissolved elements (Fe, Ni, Cr, Mo, P). Table S2 (Supporting Information) shows the amounts of dissolved elements after the accelerated degradation test. Three important facts are visible: i) the quantity of nickel dissolved is either zero or below the detection limit ii) in the stainless steel electrode (without Fe BMG layers) the Cr dissolved to great extent (from zero to 10.1 μg L^{-1}) iii) the quantity of dissolved elements increases as the number of layer increases.

3. Conclusion

The electrochemical performance of Fe-based BMG electrodes was evaluated for the OER in 0.1 M NaOH. We investigated the relationship between the number of deposited layers of additively manufactured $Fe_{75}Mo_{14.3}Ni_{1.6}P_6C_{2.2}B_1$ metallic glass, the applied process parameters, the properties of the layers, and the electrochemical activity. Higher energy densities of the applied exposure settings show better interfacial bonding between the stainless steel substrate and the glass-forming alloy. Intermixing of both compositions occurs within the first 75 μm, thus a coating thickness of five layers of 20 μm appears sufficient for the investigated process parameters. Electrodes with different thicknesses of Fe-BMG show differing activity for the OER in alkaline media. We observed that at least three conditions need to be optimized to obtain an increased activity: crystallinity, conductivity, and surface area. The presence of the glassy alloy generally increases the electrocatalytic activity compared to the steel substrate. Apparently, the defects in the applied layers become an increasingly important factor with a higher number of layers. Consequently, the active surface area obviously becomes larger. The interplay of these conflicting factors results in a discontinuous impact of the layer thickness for the BMG catalyst on the OER activity. This emphasizes the importance of furthering the understanding of the relationship between the surface state and electrochemical properties on a fundamental level. Finally, although certain amorphous materials have been considered more active than their crystalline counterpart, we observe, that this may not always be the case when other factors come into play in complex materials such as BMGs. In order to better understand the electrocatalytic properties of metallic glasses, exact and quantitative methods for determining the electrochemical surface area, crystallinity level, and the underlying mechanisms of the observed phenomena will be subject in future work. The long-term stability of this type of materials as well the reconstruction processes undergo is a challenge that needs to be addressed in order to fully understand the behavior of metallic glasses.[78,75]

4. Experimental Section

Bulk Metallic Glass Electrode Fabrication: The electrodes were prepared through PBF-LB/M using an industrial EOS M100 system (eos GmbH, Germany). The machine is equipped with a 1064 nm fiber laser with a focus diameter of ≈40 μm. Air Liquide Arcal Prime Argon (99.998 vol%) was used as shielding gas during processing with a residual oxygen content in the chamber below 0.1 vol%. The cylindrical samples were processed in a hybrid approach as illustrated in **Figure 10**.
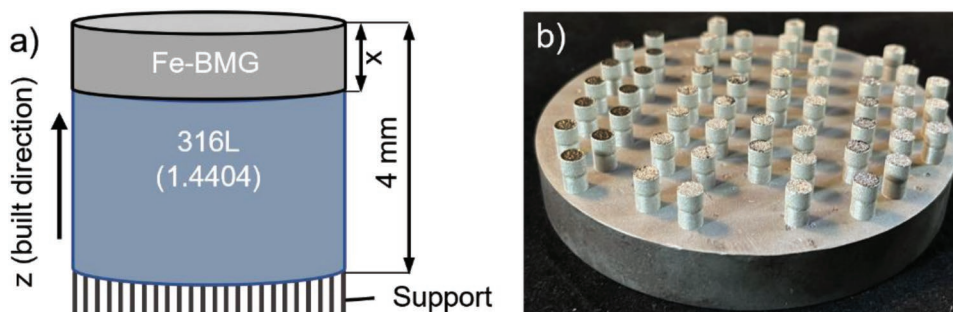
Figure 10. A) illustration of the sample geometry. B) Image of the processed samples Fe-BMG/316L.

Table 2. Overview of the processed sample geometry and the applied PBF-LB/M process parameters.

Geometric variation		Parameter variation		
Z [mm]	Number of layers [–]	Laser power P [W]	Scan speed v [m s^{-1}]	Line energy density E_L [J m^{-1}]
0.1	5	40 (const.)	1	40
0.2	10		1.5	26.67
0.3	15		2.0	20

First, stainless steel cylinders with support structures were processed by PBF-LB/M using default process parameters. Gas atomized 316L (Printdur 4404, Deutsche Edelstahl Werke Specialty Steel GmbH & Co. KG) was used with particle size d_{50} of 47.3 µm. Subsequently, the 316L powder was removed from the chamber and powder tank and replaced by the glass-forming Fe$_{75}$Mo$_{14.3}$Ni$_{1.6}$P$_6$C$_{2.2}$B$_1$ (in wt%) powder. The material was also gas atomized and provided by the Deutsche Edelstahl Werke Specialty Steel GmbH & Co. KG. The glass-forming electrode surface was then manufactured on top of the 316L substrates in four nominal heights "x" from 0.1 to 0.3 mm with a z-increment (layer thickness) of 20 µm, corresponding with 5–15 layers as summarized in **Table 2**. Additionally, three different line energy densities E_L (which is defined by $E_L = P/v$ (J m^{-1})) were evaluated throughout the experiment. Therefore, the scan speed was varied from 12 m s^{-1} at a constant laser power (P) of 40 W. The applied hatch distance between two vectors was held constant at 40 µm.

Physicochemical Characterization: Microsections of one sample for each setting were prepared orthogonal to the build direction. The respective samples were cut, embedded, sanded, and finally polished down with a 1 µm abrasive solution. Light optical microscopy (LOM) was conducted with an Olympus BX51M. SEM images were taken on a JEOL JSM-IT500LV using a backscattered electron and secondary electron detector at an acceleration voltage of 20 kV and a WD of 10 mm. Additionally, differential scanning calorimetry (DSC) of the initial powder was conducted using a Mettler Toledo DSC1 at a heating rate of 20 K min^{-1} in alumina crucibles in a temperature range from 50 to 580 °C. Additionally, the sample surfaces were analyzed through XRD Analysis using PANalytical Empyrean using the Kα-radiation of Cu with a wavelength of 1.5406 Å X-ray.

Electrochemical Characterization: The electrochemical experiments were performed using a VSP-3e potentiostat (Bio-Logic Instruments, France) computer-controlled using EC-Lab Software. All electrochemical experiments were performed under static conditions. EIS measurements were used to determine the value of the uncompensated resistance for iR-drop correction. For EIS measurement a 4 µF shunt capacitor was connected between the counter electrode and the reference electrode to avoid artifacts at high frequencies.[79] The obtained EIS spectra were then fitter to appropriate equivalent electric circuits to extract the uncompensated resistance (see Figure S10, Supporting Information). The experiment was carried out in a conventional three-electrode cell using a graphite rod counter electrode and a self-made, calibrated, RHE reference electrode (all the potentials are reported using this scale). All solutions were prepared using ultrapure water from a Millipore (Merck Millipore, Mill-Q IQ 7003) (18.2 MΩ cm), and NaOH (Merck, Suprapur). Before experiments, the electrochemical cells were cleaned with a 0.1 m KMnO$_4$ and 0.5 m H$_2$SO$_4$ mixture solution over night; afterwards all parts were rinsed with a diluted piranha solution to remove the excess permanganate and traces of manganese oxides. Finally, all the parts are boiled in ultrapure water six times. The electrochemical activity of the samples was also evaluated after a heat treatment, which leads to de-vitrification, that consist in put the samples in a horizontal tube furnace (Carbolite EHA 12/450B) heating the electrode at a rate of 0.33 K s^{-1} until 600 °C (under argon atmosphere) and maintain the electrode at the target temperature for 15 min, after which, the electrode is allowed to cool down in the same atmosphere (the cool down process take around 10 h). The electrochemical experiments were repeated three times using fresh electrodes for each run.

Supporting Information

Supporting Information is available from the Wiley Online Library or from the author.

Conflict of Interest

The authors declare no conflict of interest.

Data Availability Statement

The data that support the findings of this study are available from the corresponding author upon reasonable request.

[1] T. Reier, H. N. Nong, D. Teschner, R. Schlögl, P. Strasser, *Adv. Energy Mater.* **2017**, *7*, 1601275.

[2] A. Aijaz, J. Masa, C. Rösler, W. Xia, P. Weide, A. J. R. Botz, R. A. Fischer, W. Schuhmann, M. Muhler, *Angew. Chem., Int. Ed.* **2016**, *55*, 4087.

[3] I. Katsounaros, S. Cherevko, A. R. Zeradjanin, K. J. J. Mayrhofer, *Angew. Chem., Int. Ed.* **2014**, *53*, 102.

[4] Y. Gorlin, T. F. Jaramillo, *J. Am. Chem. Soc.* **2010**, *132*, 13612.

[5] L. Trotochaud, J. K. Ranney, K. N. Williams, S. W. Boettcher, *J. Am. Chem. Soc.* **2012**, *134*, 17253.

[6] R. Subbaraman, D. Tripkovic, K. C. Chang, D. Strmcnik, A. P. Paulikas, P. Hirunsit, M. Chan, J. Greeley, V. Stamenkovic, N. M. Markovic, *Nat. Mater.* **2012**, *11*, 550.

[7] I. C. Man, H.-Y. Su, F. Calle-Vallejo, H. A. Hansen, J. I. Martínez, N. G. Inoglu, J. Kitchin, T. F. Jaramillo, J. K. Nørskov, J. Rossmeisl, *ChemCatChem* **2011**, *3*, 1159.

[8] M. T. M. Koper, *J. Electroanal. Chem.* **2011**, *660*, 254.

**ADVANCED
SCIENCE NEWS**

www.advancedsciencenews.com

**ADVANCED
MATERIALS
INTERFACES**

Open Access

www.advmatinterfaces.de

[9] J. Masa, W. Schuhmann, *J. Solid State Electrochem.* **2020**, *24*, 2181.

[10] J. Pérez-Ramírez, N. López, *Nat. Catal.* **2019**, *2*, 971.

[11] T. Reier, M. Oezaslan, P. Strasser, *ACS Catal.* **2012**, *2*, 1765.

[12] S. Cherevko, S. Geiger, O. Kasian, N. Kulyk, J.-P. Grote, A. Savan, B. R. Shrestha, S. Merzlikin, B. Breitbach, A. Ludwig, K. J. J. Mayrhofer, *Catal. Today* **2016**, *262*, 170.

[13] Y. Matsumoto, E. Sato, *Mater. Chem. Phys.* **1986**, *14*, 397.

[14] H. Osgood, S. V. Devaguptapu, H. Xu, J. Cho, G. Wu, *Nano Today* **2016**, *11*, 601.

[15] G.-B. Wang, C.-S. Hsu, H. M. Chen, *Dalton Trans.* **2020**, *49*, 17505.

[16] T. K. Gajaria, B. Roondhe, S. D. Dabhi, P. K. Jha, *Int. J. Hydrogen Energy* **2020**, *45*, 18612.

[17] W. Li, D. Xiong, X. Gao, L. Liu, *Chem. Commun.* **2019**, *55*, 8744.

[18] J. Song, *ACS Energy Lett.* **2017**, *2*, 1937.

[19] F. P. Lohmann-Richters, S. Renz, W. Lehnert, M. Müller, M. Carmo, *J. Electrochem. Soc.* **2021**, *168*, 114501.

[20] S. H. Chang, N. Danilovic, K.-C. Chang, R. Subbaraman, A. P. Paulikas, D. W. Fong, M. J. Highland, P. M. Baldo, V. R. Stamenkovic, J. W. Freeland, J. A. Eastman, N. M. Markovic, *Nat. Commun.* **2014**, *5*, 4191.

[21] W. Cai, R. Chen, H. Yang, H. B. Tao, H.-Y. Wang, J. Gao, W. Liu, S. Liu, S.-F. Hung, B. Liu, *Nano Lett.* **2020**, *20*, 4278.

[22] V. R. Stamenkovic, D. Strmcnik, P. P. Lopes, N. M. Markovic, *Nat. Mater.* **2017**, *16*, 57.

[23] M. Calin, L. C. Zhang, J. Eckert, *Scr. Mater.* **2007**, *57*, 1101.

[24] M. Telford, *Mater. Today* **2004**, *7*, 36.

[25] F. Hu, S. Zhu, S. Chen, Y. Li, L. Ma, T. Wu, Y. Zhang, C. Wang, C. Liu, X. Yang, L. Song, X. Yang, Y. Xiong, *Adv. Mater.* **2017**, *29*, 1606570.

[26] Y. Jin, G. Xi, R. Li, Z.-A. Li, X.-B. Chen, T. Zhang, *J. Alloys Compd.* **2021**, *852*, 156876.

[27] S. Pauly, L. Löber, R. Petters, M. Stoica, S. Scudino, U. Kühn, J. Eckert, *Mater. Today* **2013**, *16*, 37.

[28] Z. Mahbooba, L. Thorsson, M. Unosson, P. Skoglund, H. West, T. Horn, C. Rock, E. Vogli, O. Harrysson, *Appl. Mater. Today* **2018**, *11*, 264.

[29] P. A. Hooper, *Addit. Manuf.* **2018**, *22*, 548.

[30] J. Wegner, M. Frey, M. Piechotta, N. Neuber, B. Adam, S. Platt, L. Ruschel, N. Schnell, S. S. Riegler, H.-R. Jiang, G. Witt, R. Busch, S. Kleszczynski, *Mater. Des.* **2021**, *209*, 109976.

[31] N. Sohrabi, J. Jhabvala, R. E. Logé, *Metals* **2021**, *11*, 1279.

[32] H. Y. Jung, S. J. Choi, K. G. Prashanth, M. Stoica, S. Scudino, S. Yi, U. Kühn, D. H. Kim, K. B. Kim, J. Eckert, *Mater. Des.* **2015**, *86*, 703.

[33] L. Thorsson, M. Unosson, M. T. Pérez-Prado, X. Jin, P. Tiberto, G. Barrera, B. Adam, N. Neuber, A. Ghavimi, M. Frey, R. Busch, I. Gallino, *Mater. Des.* **2022**, *215*, 110483.

[34] F. Xie, Q. Chen, J. Gao, *Metals* **2019**, *9*, 78.

[35] F. Xie, Q. Chen, J. Gao, Y. Li, *J. Mater. Eng. Perform.* **2019**, *28*, 3478.

[36] J. Wegner, M. Frey, S. Kleszczynski, R. Busch, G. Witt, *Proc. CIRP* **2020**, *94*, 205.

[37] J. J. Marattukalam, V. Pacheco, D. Karlsson, L. Riekehr, J. Lindwall, F. Forsberg, U. Jansson, M. Sahlberg, B. Hjörvarsson, *Addit. Manuf.* **2020**, *33*, 101124.

[38] J. P. Oliveira, A. D. LaLonde, J. Ma, *Mater. Des.* **2020**, *193*, 108762.

[39] U. Scipioni Bertoli, A. J. Wolfer, M. J. Matthews, J.-P. R. Delplanque, J. M. Schoenung, *Mater. Des.* **2017**, *113*, 331.

[40] S.-X. Liang, X. Wang, W. Zhang, Y.-J. Liu, W. Wang, L.-C. Zhang, *Appl. Mater. Today* **2020**, *19*, 100543.

[41] C. Yang, C. Zhang, L. Liu, *J. Mater. Chem. A* **2018**, *6*, 20992.

[42] Y. Liu, Y. Yang, S. Mai, D. i. Wang, C. Song, *Mater. Des.* **2015**, *87*, 797.

[43] J. Liu, Y. Song, C. Chen, X. Wang, H. Li, C. Zhou, J. Wang, K. Guo, J. Sun, *Mater. Des.* **2016**, *186*, 108355.

[44] D. Wang, C. Song, Y. Yang, Y. Bai, *Mater. Des.* **2016**, *100*, 291.

[45] N. Ciftci, N. Ellendt, E. Soares Barreto, L. Mädler, V. Uhlenwinkel, *Adv. Powder Technol.* **2018**, *29*, 380.

[46] M. E. G. Lyons, M. P. Brandon, *Int. J. Electrochem. Sci.* **2008**, *3*, 1463.

[47] R. L. Doyle, M. E. G. Lyons, *J. Electrochem. Soc.* **2013**, *160*, H142.

[48] V. Čolić, J. Tymoczko, A. Maljusch, A. Ganassin, W. Schuhmann, A. S. Bandarenka, *ChemElectroChem* **2015**, *2*, 143.

[49] V. Lubkowitz, J. Alber, F. Zanger, *Materials* **2021**, *14*, 6665.

[50] P. Fathi-Hafshejani, A. Soltani-Tehrani, N. Shamsaei, M. Mahjouri-Samani, *Addit. Manuf.* **2022**, *50*, 102572.

[51] M. S. Burke, S. Zou, L. J. Enman, J. E. Kellon, C. A. Gabor, E. Pledger, S. W. Boettcher, *J. Phys. Chem. Lett.* **2015**, *6*, 3737.

[52] R. E. Hummel, in *Electronic Properties of Materials*, (Ed: R. E. Hummel), Springer, New York **2011**, p. 181.

[53] R. E. Hummel, in *Electronic Properties of Materials*, (Ed: R. E. Hummel), Springer, New York **2011**, p. 79.

[54] J. Timoshenko, F. T. Haase, S. Saddeler, M. Rüscher, H. S. Jeon, A. Herzog, U. Hejral, A. Bergmann, S. Schulz, B. R. Cuenya, *J. Am. Chem. Soc.* **2023**, *145*, 4065.

[55] E. Budiyanto, S. Salamon, Y. Wang, H. Wende, H. Tüysüz, *JACS Au* **2022**, *2*, 697.

[56] D. A. Lutterman, Y. Surendranath, D. G. Nocera, *J. Am. Chem. Soc.* **2009**, *131*, 3838.

[57] M. Görlin, J. Halldin Stenlid, S. Koroidov, H.-Y. Wang, M. Börner, M. Shipilin, A. Kalinko, V. Murzin, O. V. Safonova, M. Nachtegaal, A. Uheida, J. Dutta, M. Bauer, A. Nilsson, O. Diaz-Morales, *Nat. Commun.* **2020**, *11*, 6181.

[58] P. Connor, J. Schuch, B. Kaiser, W. Jaegermann, *Z. Physik. Chem.* **2020**, *234*, 979.

[59] D. M. Morales, M. Risch, *J. Phys. Energy* **2021**, *3*, 34013.

[60] C. C. L. McCrory, S. Jung, J. C. Peters, T. F. Jaramillo, *J. Am. Chem. Soc.* **2013**, *135*, 16977.

[61] D. M. Kolb, *Prog. Surf. Sci.* **1996**, *51*, 109.

[62] P. Castelli, S. Trasatti, F. H. Pollak, W. E. O'Grady, *J. Electroanal. Chem. Interfacial Electrochem.* **1986**, *210*, 189.

[63] O. Diaz-Morales, F. Calle-Vallejo, C. de Munck, M. T. M. Koper, *Chem. Sci.* **2013**, *4*, 2334.

[64] E. Özer, C. Spöri, T. Reier, P. Strasser, *ChemCatChem* **2017**, *9*, 597.

[65] K. A. Stoerzinger, O. Diaz-Morales, M. Kolb, R. R. Rao, R. Frydendal, L. Qiao, X. R. Wang, N. B. Halck, J. Rossmeisl, H. A. Hansen, T. Vegge, I. E. L. Stephens, M. T. M. Koper, Y. Shao-Horn, *ACS Energy Lett.* **2017**, *2*, 876.

[66] Y. Zhou, H. J. Fan, *ACS Mater. Lett.* **2021**, *3*, 136.

[67] X. Wang, W. Ma, C. Ding, Z. Xu, H. Wang, X. Zong, C. Li, *ACS Catal.* **2018**, *8*, 9926.

[68] J. Park, S. Lee, S. Kim, *Front. Chem.* **2022**, *10*, 1024865.

[69] J. Bak, T. G. Yun, J.-S. An, H. B. Bae, S.-Y. Chung, *Energy Environ. Sci.* **2022**, *15*, 610.

[70] S. Anantharaj, M. Venkatesh, A. S. Salunke, T. V. S. V. Simha, V. Prabu, S. Kundu, *ACS Sustainable Chem. Eng.* **2017**, *5*, 10072.

[71] M. Chatenet, B. G. Pollet, D. R. Dekel, F. Dionigi, J. Deseure, P. Millet, R. D. Braatz, M. Z. Bazant, M. Eikerling, I. Staffell, P. Balcombe, Y. Shao-Horn, H. Schäfer, *Chem. Soc. Rev.* **2022**, *51*, 4583.

[72] F.-Y. Chen, Z.-Y. Wu, Z. Adler, H. Wang, *Joule* **2021**, *5*, 1704.

[73] F. Moureaux, P. Stevens, G. Toussaint, M. Chatenet, *Appl. Catal., B* **2019**, *258*, 117963.

[74] H. Schäfer, M. Chatenet, *ACS Energy Lett.* **2018**, *3*, 574.

[75] H. Schäfer, K. Küpper, M. Schmidt, K. Müller-Buschbaum, J. Stangl, D. Daum, M. Steinhart, C. Schulz-Kölbel, W. Han, J. Wollschläger, U. Krupp, P. Hou, X. Liu, *Catal. Sci. Technol.* **2018**, *8*, 2104.

[76] F. Moureaux, P. Stevens, G. Toussaint, M. Chatenet, *J. Power Sources* **2013**, *229*, 123.

[77] W. Han, K. Kuepper, P. Hou, W. Akram, H. Eickmeier, J. Hardege, M. Steinhart, H. Schäfer, *ChemSusChem* **2018**, *11*, 3661.

[78] H. Schäfer, M. Chatenet, *ACS Energy Lett.* **2018**, *3*, 574.

[79] S. Watzele, P. Hauenstein, Y. Liang, S. Xue, J. Fichtner, B. Garlyyev, D. Scieszka, F. Claudel, F. Maillard, A. S. Bandarenka, *ACS Catal.* **2019**, *9*, 9222.